



An earth mover's distance based multivariate generalized likelihood ratio control chart for effective monitoring of 3D point cloud surface

Chen Zhao^a, Chun Fai Lui^b, Shichang Du^{a,*}, Di Wang^a, Yiping Shao^c

^a Department of Industrial Engineering and Management, School of Mechanical Engineering, Shanghai Jiao Tong University, Shanghai, China

^b Department of Advanced Design and Systems Engineering, City University of Hong Kong, Hong Kong

^c College of Mechanical Engineering, Zhejiang University of Technology, Zhejiang, China

ARTICLE INFO

Keywords:

3D surface monitoring
Point cloud
High-definition measurement
Control chart
Earth mover's distance

ABSTRACT

With the development of measurement technology, non-contact high-definition measurement (HDM) systems have allowed rapid collection of large-scale point cloud data, providing an opportunity to monitor the entire surface geometry of manufactured parts. However, traditional control charts do not apply to such large-scale point cloud data. Although some researchers have proposed the use of improved multivariate control charts for high-dimensional data, the multivariate control charts cannot be directly used for large-scale and auto-correlated point cloud data. Considering the structural characteristics and spatial properties of the point cloud, this paper proposes an earth mover's distance based multivariate generalized likelihood ratio (EMD-MGLR) control chart to effectively monitor point cloud surface by making full use of the three-dimensional (3D) information of point cloud data. The EMD method regards point cloud data as a distribution and calculates the EMD distance between the two distributions to quantify the deviation region between the point cloud surface and the nominal model. Combined with the multivariate generalized likelihood ratio control chart, the processing quality of the 3D surface can then be monitored by the statistics of EMD. The advantages of the proposed method are illustrated and verified by numerical and experimental examples. An experimental example on the 3D surfaces of combustion chambers is used to illustrate the methodology and to test its effectiveness in monitoring surface defects.

1. Introduction

In modern manufacturing, the surface form of some precision parts has an important influence on the overall quality of the part. However, due to the arbitrariness and complexity of three-dimensional (3D) surfaces, it is difficult to evaluate and monitor the surface defects through limited measurement points. Recent advancements in non-contact high-definition measurement (HDM) systems have provided new opportunities in manufacturing and have been widely applied in many areas such as 3D inspection (Zhao et al., 2022), surface topography analysis (Yin et al., 2020; Du et al., 2015), and precision machining (Zhao, Cheung, & Liu, 2019). In particular, optical scanner systems are one of the HDM systems for surface detection, which can collect large-scale point cloud data in minutes and represent entire geometrical information for measuring surfaces. The advantages of high efficiency, high density, and large scenes make optical scanner systems useful for

inspecting parts with complex surface geometries.

Compared with traditional contact acquisition systems, the point cloud generated by an optical scanner can fully reflect surface information, thereby providing a data basis for 3D surface description and quality control. Fig. 1 shows the high-density point cloud data of engine cylinder head combustion chamber obtained by 3D linear laser scanning. The inner surface of combustion chamber is a complex 3D curved surface and affects the performance of the engine. The high-density point cloud data obtained by HDM can completely reflect the entire surface geometry of the combustion chamber, providing opportunities for online inspection and quality control of curved surfaces.

To monitor and control the quality of manufacturing parts, control chart is commonly used as an efficient, powerful tool for statistical process control (SPC) in modern manufacturing. However, large-scale point cloud data of 3D curved surfaces are out of the scope of traditional control charts, bringing challenges to online monitoring of surface

* Corresponding author.

E-mail addresses: zhao_chen@sjtu.edu.cn (C. Zhao), chunflui5-c@my.cityu.edu.hk (C.F. Lui), lovbin@sjtu.edu.cn (S. Du), d.wang@sjtu.edu.cn (D. Wang), syp123gh@zjut.edu.cn (Y. Shao).

<https://doi.org/10.1016/j.cie.2022.108911>

Received 19 October 2022; Accepted 11 December 2022

Available online 15 December 2022

0360-8352/© 2022 Elsevier Ltd. All rights reserved.

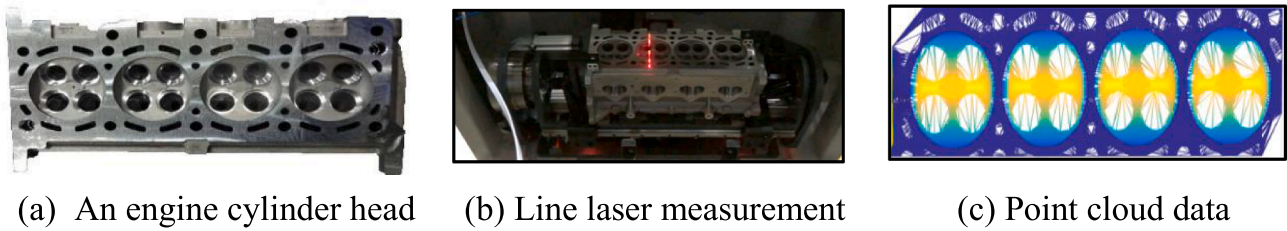


Fig. 1. The 3D line laser scanning point cloud data of engine cylinder head.

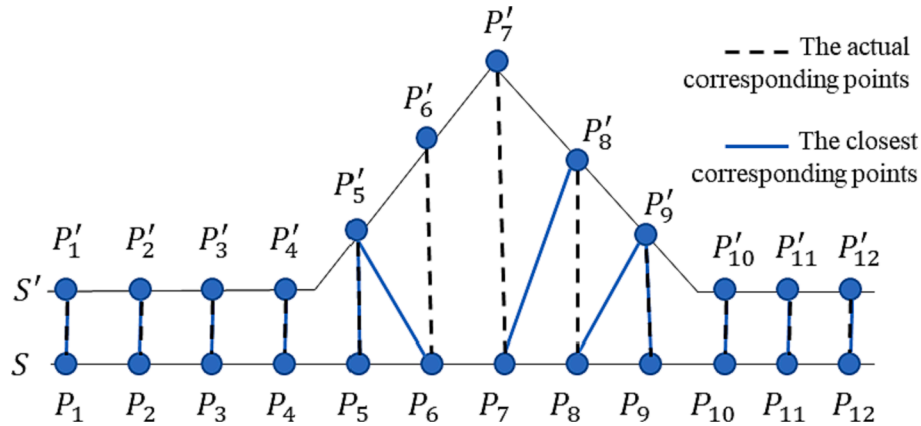


Fig. 2. The comparison of the closest points and actual corresponding points.

quality. Recently, research on multivariate control charts for monitoring high-dimensional data have received extensive attention (Wells et al. 2013; Shu and Fan, 2018; Zhang et al., 2019; Mukherjee and Marozzi, 2021). These methods consider multiple correlated quality characteristics to rapidly detect process changes. But for large-scale and high autocorrelation point cloud data, the information of point cloud is neglected as it cannot be used directly in the current control charts. To this end, the point cloud data must be processed and summarized in a way that does not lose valuable information (Stankus et al., 2019).

In addition, only a few quantitative studies have been carried out on the monitoring of point cloud data up to date, especially for 3D curved surfaces. For curved surface point clouds, it is difficult to describe an irregular surface by one or several features due to the complexity and arbitrariness of the surface shape. Nevertheless, when the shape of the surface is complex, non-parametric method can significantly reduce the complexity of the calculation. Therefore, non-parametric control charts have received increasing attention for efficient monitoring of 3D curved surfaces. Such methods can be divided into three types: scale model method, dimensionality reduction method, and spatial distance method.

The scale model method compares the difference between the measurement sample and the reference sample using the given metric. Williams et al. (2007) proposed the basic flow and the metrics of this method. First, the reference sample is obtained by calculating the average value of the sample profiles. Based on the basic sample profile, they proposed five metrics to measure the degree of profile deviation. Also, Jia et al. (2021) performed piecewise fitting on the point clouds of cylinders and monitored the structural deformation by the relative inclination. In general, a scale model method monitors processes based on surface feature extraction, resulting in loss of surface information.

For complex nonlinear data, the dimensionality reduction method maps the data points in the original high-dimensional space to the low-dimensional space for ease of computation. He et al. (2017) projected 3D point clouds into two-dimensional (2D) grayscale images and monitored the images via a multivariate generalized likelihood ratio (MGLR) control chart. Likewise, Colosimo and Tajbakhsh (2014) mapped a 3D

surface onto a 2D manifold structure through ISOMAP and performed parametric reconstruction of the 3D surface. In addition, Wells et al. (2013) transformed high-dimensional data into linear contours through the Q-Q plot method to reflect the relationship between the measurement sample and the benchmark sample. Furthermore, Pacella and Colosimo (2018) used multilinear principal component analysis to reduce the dimensionality of multidimensional data arrays. However, the dimensionality reduction method inevitably causes deformation of the spatial structure, destroys relevant structures in the original data, and suffers from information loss problems (Yan, Paynabar, & Pacella, 2019).

Unlike scale model method and dimensionality reduction method, the spatial distance method measures the variability of the sample by calculating the distance between the sample and the nominal surface. Stankus and Castillo-Villar (2019) calculated the deviation of the measurement points from standard Computer Aided Design (CAD) and applied the MGLR control chart to monitor the regions of interest (ROIs). However, this method requires a known nominal surface CAD model. Zang and Qiu (2018a, 2018b) calculated translation and rotation matrices of measurement points to monitor 3D printing surface quality. The method can be applied to arbitrary 3D surfaces with regular and sparse measurements but is computationally expensive for point cloud data. Scimone et al. (2021) used Hausdorff distance to monitor point cloud samples with spatial structure changes. The spatial distance method does not need to deform the original data and can preserve more of the original information than the other two methods.

In general, for the monitoring of 3D surfaces, the existing scale model methods and dimensionality reduction methods are unable to process point cloud data directly and difficult to guarantee the spatial structure of arbitrary 3D surfaces. In contrast, the spatial distance method can directly process point cloud data and has advantages for efficient calculation of large-scale data. However, existing spatial distance methods are offset-based distance functions. Based on the closest point hypothesis, the closest point in the two-point cloud is considered as the corresponding point in these methods. As distances increase, the dis-

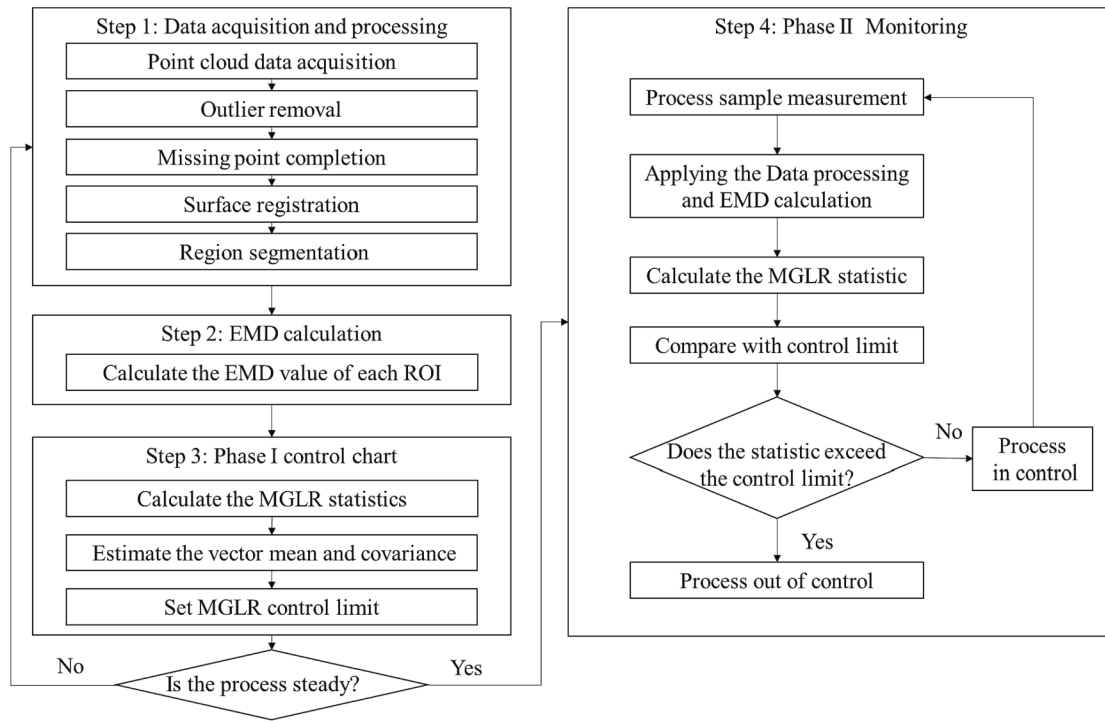


Fig. 3. Flowchart of the proposed method.

tance does not conform to geometric characteristics (Solomon et al., 2014; Chazal, Cohen-Steiner, & Mérigot, 2010). A graphical illustration is shown in Fig. 2. In Fig. 2, consider S and S' are two corresponding scan lines on two surfaces, the coordinate points P and P' are in one-to-one correspondence, the black dotted line is the actual corresponding points, and the blue solid line is the closest corresponding points. It can be seen that as the deviation between S and S' increases, the error in calculating the distance between S and S' based on the nearest point principle will be large, and some point cloud information is not used (such as P'_6 and P'_7).

Regarding this problem, this paper explores a general 3D point cloud surface monitoring method, which can make full use of the 3D information of point cloud. Based on the basic principle of the spatial distance method, an Earth Mover's Distance (EMD) based control chart is proposed to calculate the point cloud distance between the measured sample and the nominal sample. The EMD method finds the best mapping function from one set to the other by solving an optimization problem, thus provides a one-to-one correspondence between points in the two point clouds. The advantage of this method is that it can fully consider the information of all points on the point cloud and summarize them as EMD distance, which is sensitive to details and the density distribution. In order to quickly identify the process shifts and locate the position of surface defects, a multivariate generalized likelihood ratio (MGLR) based monitoring method, namely earth mover's distance based multivariate generalized likelihood ratio (EMD-MGLR) control chart, is proposed for effective and efficient monitoring of 3D point cloud surfaces in the case where large-scale line laser point clouds are available. The remainder of this paper is organized as follows. Section 2 describes the proposed EMD-MGLR method. Sections 3 and 4 demonstrate the proposed EMD-MGLR with numerical simulations and practical studies. Finally, Section 5 presents the conclusions and discusses the implications for future research.

2. The proposed method

2.1. Framework

In this paper, an EMD-MGLR method is proposed to monitor 3D point cloud surfaces. The construction of the proposed EMD-MGLR control chart is briefly described as follows. First, the measurement point cloud is collected, preprocessed and divided into ROIs. Second, the EMD value of each ROI for the measured samples is calculated. Finally, the MGLR control chart is developed for Phase I and Phase II monitoring. In Phase I, the qualified samples are collected to compute control limits and set up the EMD-MGLR control chart. In Phase II, the EMD-MGLR control chart is used for monitoring the process stability and identifying the process shifts. A flowchart that summarizes the construction procedure of the proposed EMD-MGLR method is shown in Fig. 3.

From Fig. 3, the framework of the proposed EMD-MGLR method consists of the following four main steps:

Step 1: Data acquisition and preprocessing. The measured point cloud data is preprocessed by outlier removal, missing point completion, and surface registration. Then, according to the size and shape of point cloud surface, the 3D volume space of the sample is divided into ROIs.

Step 2: EMD calculation. EMD value represents the differences between two registered point clouds. Based on the general definition of the EMD between two subsets of a metric space, the distance representation of each ROI of the measurement sample and the nominal sample is calculated.

Step 3: Phase I control chart. The Phase I control chart is designed by the qualified samples of the in-control process based on MGLR. According to the EMD values of the measured samples, the in-control mean vector and covariance matrix are estimated to compute the statistics. The control limit is set through the simulation. If the process is steady, the parameter values and control limit are retained by simulation. If the process is unsteady, recapture samples from the first step until the process is steady.

Step 4: Phase II monitoring. Phase II process monitoring is performed to identify process shifts and provide feedback to the manufacturing process. The sample statistic is compared with the control limit. If the

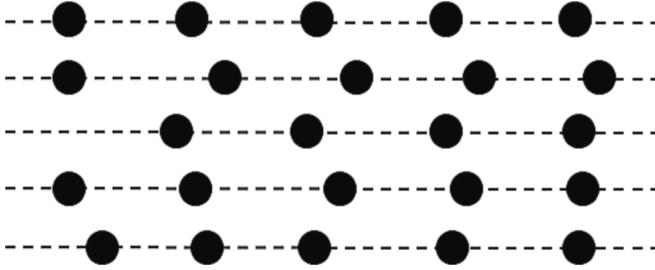


Fig. 4. Point cloud of scanning lines.

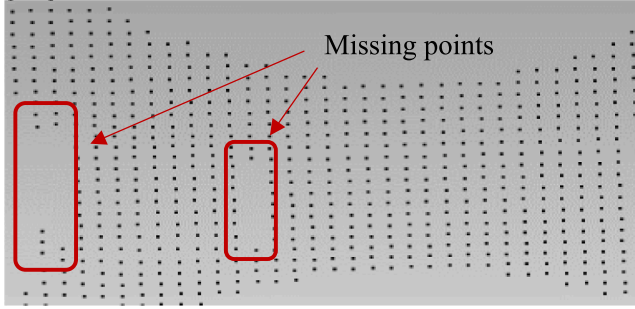


Fig. 5. Missing points in a measured point cloud.

statistic exceeds the control limit, the sample is unqualified and the process is out of control. If the statistical data does not exceed the control limit, the process is in control, and the next sample is measured and computed according to this process.

2.2. Data preprocessing and regional division

In the data acquisition, the point cloud obtained by 3D line laser is of scanning line type, as shown in Fig. 4. In data preprocessing, outlier removal, missing point completion, surface registration, and region segmentation are required for point clouds.

(1) Outlier removal

Due to the influence of the measurement environment, the point cloud data obtained by 3D line laser are contaminated with measurement noise. In order to filter the measurement noise, point cloud filtering is usually used to remove obvious outliers by calculating the average distance from each point to its k nearest points. Since the outlier points are sparsely distributed in space, the points outside the variance can be eliminated according to the given mean and variance.

(2) Missing point completion

Missing points are common in the point cloud due to the measurement loss and outlier removal (as shown in Fig. 5). Therefore, it is necessary to complete the measurement points to ensure the integrity of the point cloud. The missing points are marked as null values and can be filled by the coordinate interpolation method based on the neighborhood points.

(3) Surface registration

If the measurement centers are inconsistent, measurement samples need to be aligned with the nominal sample. The Principal Component Analysis (PCA) method (c.f. Zhao et al., 2021) can be used for rough registration, and the Iterative Closest Point (ICP) method (proposed by Besl & McKay, 1992) can be used for fine registration. The residual

deviation after registration is relatively small with respect to the surface differences and can be included in the variability of the measured surface (Scimone et al., 2021). The calculated distance can be regarded as the error value between the surface of the measurement sample and the nominal sample.

(4) Region segmentation

To summarize the deviation of point cloud data, ROIs are defined according to the shape and size of the point cloud surface. Megahed et al. (2012) restricted the ROIs to be square-shaped and overlapping. He et al. (2017) converted 3D point clouds into 2D gray images and divided the images into squares, non-overlapping ROIs. Stankus and Castillo-Villar (2019) divided 3D point clouds into ROIs in three directions. In this paper, the point cloud is segmented in the form of non-overlapping cubes.

2.3. Point cloud distance calculation based on EMD

In this method, point cloud data is regarded as a sampling of an unknown compact subset K of Euclidean space. The minimum distance between a point x in \mathbb{R}^d and any point in set K can be calculated by the distance function $d_K : \mathbb{R}^d \rightarrow \mathbb{R}$, which maps the point x to K . To solve this problem, the probability distribution is introduced to the distance function. Considering the distance between point clouds as the distance between two measures, the concept is robust to outliers. The distance between the two measures can be measured by EMD, which quantifies the cost of best transporting one measure to the other.

EMD is a method to measure image similarity proposed by Rubner et al. (1998) and was originally used for image retrieval. Due to its advantages (e.g., it avoids the quantification problems of most other measures), EMD has been used in similarity measures to measure the dissimilarity between two multidimensional distributions. EMD reflects the minimal cost of converting one signature to another. It is based on the transportation problem and can be formalized as the following linear programming problem. There are two sets of distributions: The first signature is $P = \{(p_1, w_{p1}), \dots, (p_m, w_{pm})\}$, where w_{pi} is the weight of the feature p_i and $i = 1 \dots m$. The second signature is $Q = \{(q_1, w_{q1}), \dots, (q_m, w_{qn})\}$, where w_{qj} is the weight of the feature q_j and $j = 1 \dots n$. $D = [d_{ij}]$ represents the distance matrix, where d_{ij} represents the distance between p_i and q_j . The goal of the EMD method is to find a flow $F = [f_{ij}]$ that minimizes the work required to move earth from P to Q .

$$F^* = \underset{F}{\operatorname{argmin}} \operatorname{WORK}(P, Q, F) = \underset{F}{\operatorname{argmin}} \left(\sum_{i=1}^m \sum_{j=1}^n f_{ij} d_{ij} \right) \quad (1)$$

$$\text{s.t. } f_{ij} \geq 0$$

$$\sum_{j=1}^n f_{ij} \leq w_{pi}$$

$$\sum_{i=1}^m f_{ij} \leq w_{qj}$$

$$\sum_{i=1}^m \sum_{j=1}^n f_{ij} = \min \left(\sum_{i=1}^m w_{pi}, \sum_{j=1}^n w_{qj} \right)$$

The first constraint allows the flow only from P to Q , but not in reverse. The second and third constraints limit the amount of supply, which needs to be no greater than each weight w . The fourth constraint guarantees the maximum value of reasonable transportation.

F^* can be solved by linear programming, and the EMD value is calculated as.

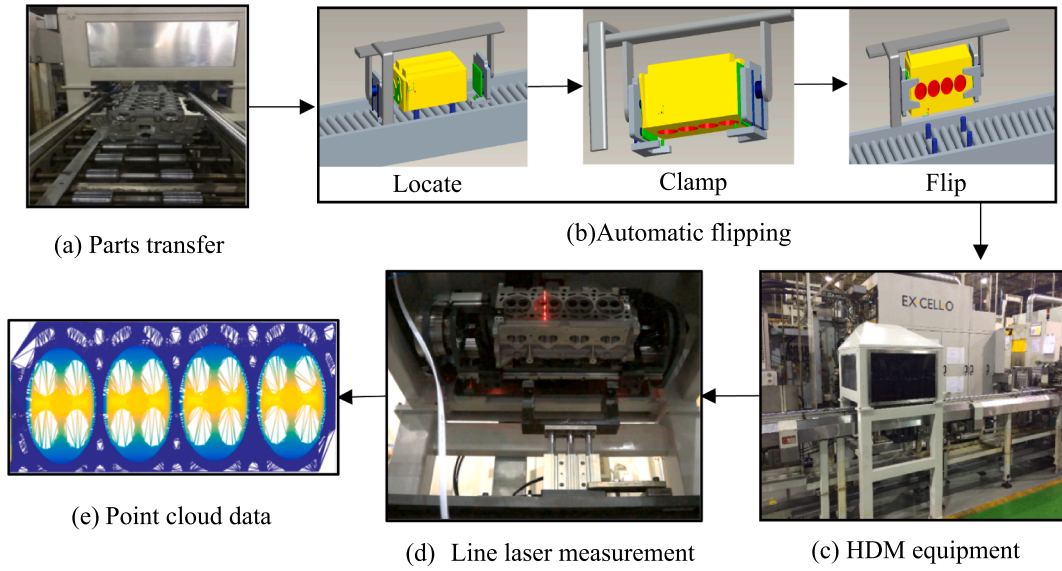


Fig. 6. The measurement process of cylinder head.

$$EMD(P, Q) = \frac{\sum_{i=1}^m \sum_{j=1}^n f_{ij} d_{ij}}{\sum_{i=1}^m \sum_{j=1}^n f_{ij}} \quad (2)$$

The EMD method can be extended to the point cloud distance calculation. Let P represents the first point cloud $\{p_1, \dots, p_i, \dots, p_m\}$ with m points. p_i is the 3D coordinate of the i th point in P . $\{w_{p1}, \dots, w_{pm}\}$ represents the weight of each point (all are equal to 1); Q represents the second point cloud $\{q_1, \dots, q_j, \dots, q_n\}$ with n points. q_j is the 3D coordinate of the j th point in Q . $\{w_{q1}, \dots, w_{qn}\}$ represents the weight of each point (all are equal to 1). $D = [d_{ij}]$ represents the distance (e.g., the Euclidean distance) from the i th point of P to the j th point of Q . $F = [f_{ij}]$ is 0 or 1, indicating whether to move the i th point of P to the j th point of Q . Then, $WORK(P, Q, F)$ represents the total cost of moving points in P to points in Q .

The measure representation of the point cloud P and Q is expressed as: $P = \frac{1}{|P|} \sum_{x \in P} \delta_x$ and $Q = \frac{1}{|Q|} \sum_{y \in Q} \delta_y$, where δ_x denotes the Dirac delta distribution of point x in P . P is taken as the point cloud to be labeled, and Q is the nominal sample. For the k th corresponding ROI of P and Q , the EMD value is calculated as.

$$EMD(P_k, Q_k) = \min_{\phi: P_k \rightarrow Q_k} \frac{1}{|P_k|} \sum_{x \in P_k} \|x - \phi(x)\|_2 \quad (3)$$

where ϕ is a bijection, x is a point in point cloud P , and k is the k th ROI corresponding to P and Q . This optimization problem is a transportation problem, which can be effectively solved by the simplex method. The EMD values can be regarded as the quality statistics of a sample, and so the surface monitoring can be transformed into the multivariate control chart of EMD values.

2.4. The MGLR control chart for the monitoring

MGLR is an effective method to establish a multivariate control chart. It can detect shifts more quickly and is more convenient compared to other multivariate control charts, such as multivariate exponentially weighted moving average and multivariate cumulative sum control charts (Wang & Reynolds, 2013). Therefore, the MGLR control chart is used to monitor the EMD values of point clouds.

For the i th sample, the EMD values are arranged in vector order: $X_i = (x_{i1}, \dots, x_{ip})$ where x is the EMD value of a region, and p is the number of ROIs. Assume that the production process is continuous and a series of samples are collected. At an unknown time τ , $0 < \tau < k$, the process is

affected by abnormal factors and shifted, causing the mean value of the region to deviate from its distribution in the controlled state. As of time k , a series of samples (X_1, \dots, X_k) has been collected from the process.

Then the likelihood function at time k can be expressed as.

$$L_{\tau,k}(\mu_0, \mu_1) = \prod_{i=1}^{\tau} f(X_i | \mu_0, \Sigma_0) \times \prod_{i=\tau+1}^k f(X_i | \mu_1, \Sigma_0) \quad (4)$$

where $f()$ represents the probability density function of the multivariate normal distribution, μ is the mean vector, and Σ is the covariance matrix. Assume only the mean vector is shifted from μ_0 to μ_1 , while the covariance matrix Σ_0 remains unchanged. If the process never shifts, the likelihood function at time k can be expressed as.

$$L_{\infty,k}(\mu_0) = \prod_{i=1}^k f(X_i | \mu_0, \Sigma_0) \quad (5)$$

The statistic for the control chart is.

$$R_k = \max_{0 \leq \tau < k} \frac{\log L_{\tau,k}(\mu_0, \mu_1)}{\log L_{\infty,k}(\mu_0)} = \max_{0 \leq \tau < k} \frac{k - \tau}{2} (\hat{\mu}_{1,\tau,k} - \mu_0)' \Sigma_0^{-1} (\hat{\mu}_{1,\tau,k} - \mu_0) \quad (6)$$

where $\hat{\mu}_{1,\tau,k} = \frac{\sum_{i=\tau+1}^k X_i}{k - \tau}$ is the maximum likelihood estimate of μ_1 .

It can be seen from formula (6) that, at time k , all previous data needs to be saved to compute the value of R_k . When the value of k is large, the calculation is complicated. A moving time window approach restricts the computation to the m nearest samples, which can reduce the computation workload. The statistic of the moving time window is computed as.

$$R_{m,k} = \begin{cases} \max_{0 \leq \tau < k} \frac{k - \tau}{2} (\hat{\mu}_{1,\tau,k} - \mu_0)' \Sigma_0^{-1} (\hat{\mu}_{1,\tau,k} - \mu_0) & k = 1, 2, \dots, m \\ \max_{k-m \leq \tau < k} \frac{k - \tau}{2} (\hat{\mu}_{1,\tau,k} - \mu_0)' \Sigma_0^{-1} (\hat{\mu}_{1,\tau,k} - \mu_0) & k = m + 1, m + 2, \dots \end{cases} \quad (7)$$

When $R_{m,k}$ is greater than the control limit, the control chart issues an alarm and the process is out of control. Wang and Reynolds (2013) gave the control limit values when the number of ROIs is less than 30. When the number of ROIs is greater than 30, the control limit can be obtained by process simulation.

The control chart consists of two phases. Phases I is used to evaluate process stability and estimate control limits. Phases II is the control phase and is used for process monitoring. When the control chart gives a signal, the current sample is out of control. By comparing and analyzing

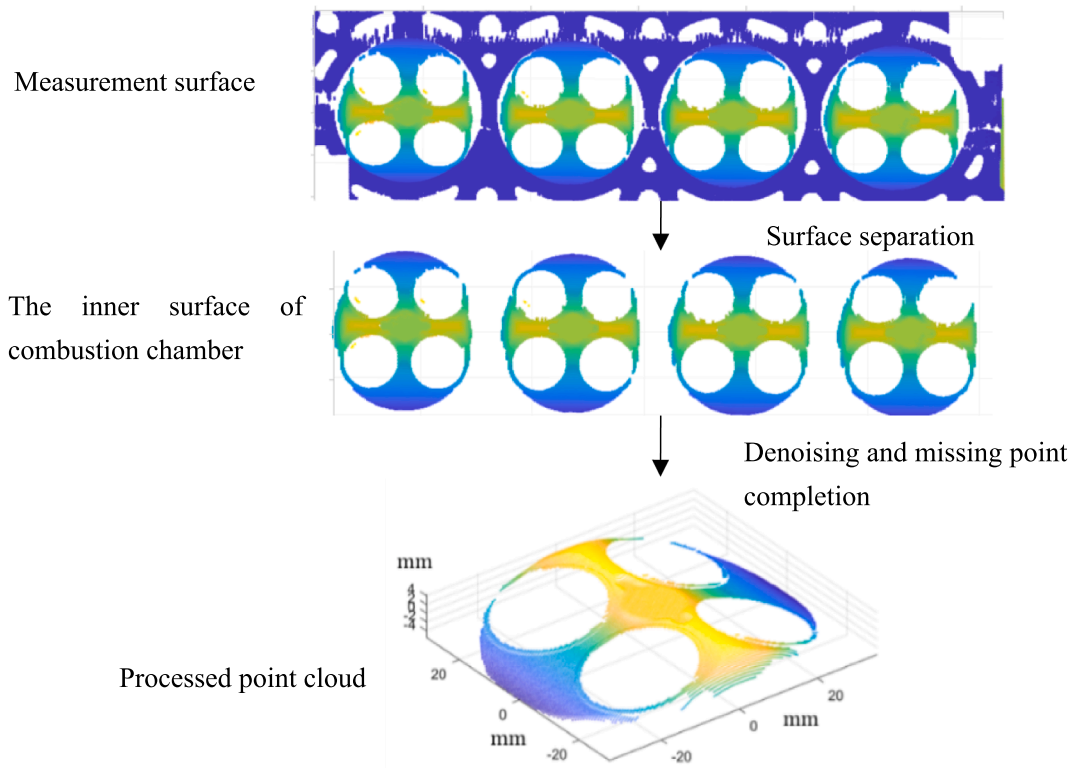


Fig. 7. The processing of measurement data.

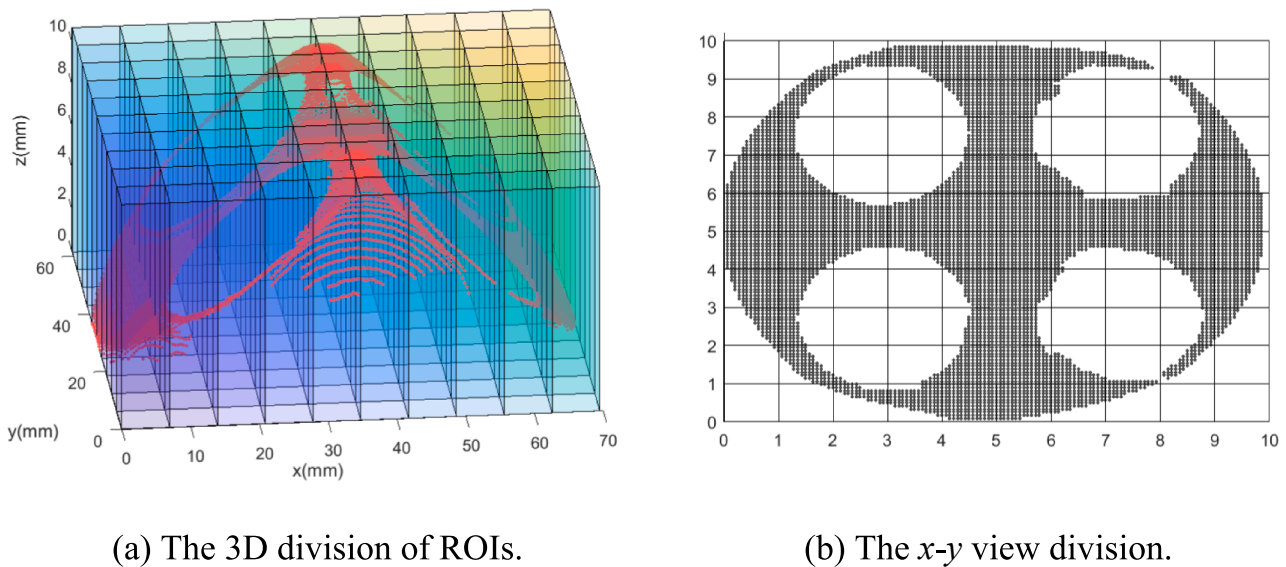


Fig. 8. The diagram of 10×10 ROIs.

the mean value of each ROI under the control and its value after the occurrence of the shift, ROIs with defects can be identified. Making full use of the information of the time and regions of the defects can help producers find the abnormal cause of the out-of-control process and take corrective measures to restore the production process to a steady state as soon as possible.

3. Experimental analysis

3.1. Experimental settings

The engine cylinder head combustion chambers are taken as examples for measurement and analysis to evaluate the application of the proposed method. The inner surface of combustion chamber is a complex 3D curved surface and is cast from a mold. The mold is in frequent contact with the casting material under high temperature conditions for a long time and is prone to wear. In turn, it affects the curved shape of the combustion chamber and the performance of the engine.

Table 1
Control limits of three ROIs.

ROI	Control limit
10 × 10	90.31
15 × 15	94.12
20 × 20	118.61

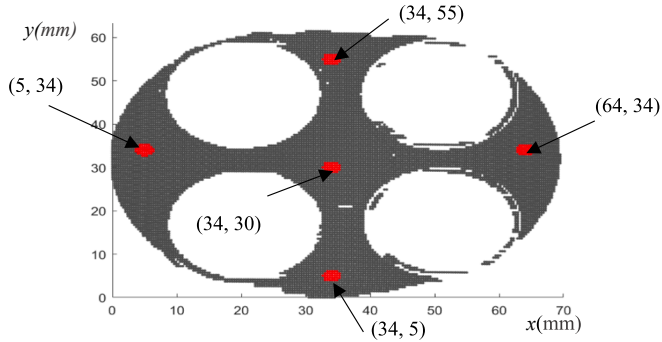


Fig. 9. The diagram of in-control point clouds with defects added.

Table 2
The comparison of ARL1 values of different ROIs.

Defect size	Location coordinate of the center	ROIs		
		10 × 10	15 × 15	20 × 20
R = 2	(34, 30)	157.23	24.38	1.75
	(34, 55)	197.62	3.74	4.58
	(34, 5)	203.75	29.62	2.34
	(5, 34)	149.88	24.97	11.09
	(64, 34)	193.41	17.98	11.25
R = 1	(34, 30)	198.72	139.23	4.03
	(34, 55)	175.68	103.45	18.36
	(34, 5)	191.31	198.62	4.85
	(5, 34)	189.07	201.60	63.77
	(64, 34)	196.09	178.88	49.55

In this experiment, a 3D line laser scanner in a HDM instrument was used to measure the surface of the combustion chamber. The HDM instrument can produce large-scale point cloud data of the scanned surface within a few minutes. Thus, it can quickly and comprehensively reflect the surface information, and it provides the data basis for the surface quality inspection of parts. The measurement process is shown in Fig. 6. Fig. 6 (a) is the transfer of the tested cylinder head on the production line. Fig. 6 (b) shows the automatic locating, clamping, and flipping of the measured cylinder head. The combustion chamber surface is upward

to be measured. Fig. 6 (c) is the HDM equipment and Fig. 6 (d) is the line laser measurement process. During the measurement, the engine cylinder head is scanned by line laser from left to right on the conveyor belt. In this instrument, each cylinder head contains 1280 laser lines and one laser line contains 640 points. The accuracy in Z is ± 0.02 mm and the resolution of the system is 0.02 mm³. This measurement error is allowable in the production process. Fig. 6 (e) shows the point cloud data measured on an engine cylinder head.

Table 3
The ARL1 values of different defects of 20 × 20 ROIs.

Defect size	Location coordinate of the center	Magnitude of shift					
		-0.3	-0.2	-0.1	+0.1	+0.2	+0.3
R = 2	(34, 30)	1.00	11.72	45.64	37.11	1.75	1.00
	(34, 55)	1.37	7.13	159.83	79.80	4.58	1.00
	(34, 5)	1.76	4.52	55.73	46.42	2.34	1.19
	(5, 34)	1.44	11.46	59.09	68.76	11.09	3.42
	(64, 34)	3.23	15.43	62.42	53.42	11.25	1.44
R = 1	(34, 30)	1.89	8.80	69.71	59.04	4.03	1.24
	(34, 55)	2.62	14.62	159.60	67.73	18.36	2.71
	(34, 5)	3.76	11.32	63.47	57.32	4.85	1.63
	(5, 34)	1.73	62.41	170.63	180.77	63.77	5.16
	(64, 34)	1.56	57.63	162.18	197.61	49.55	1.44

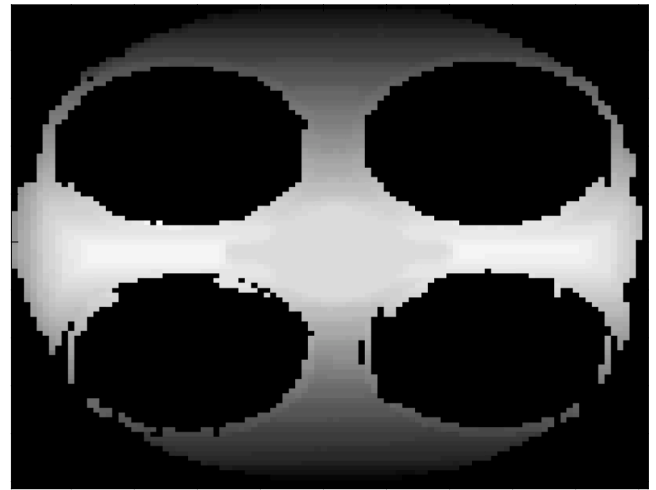
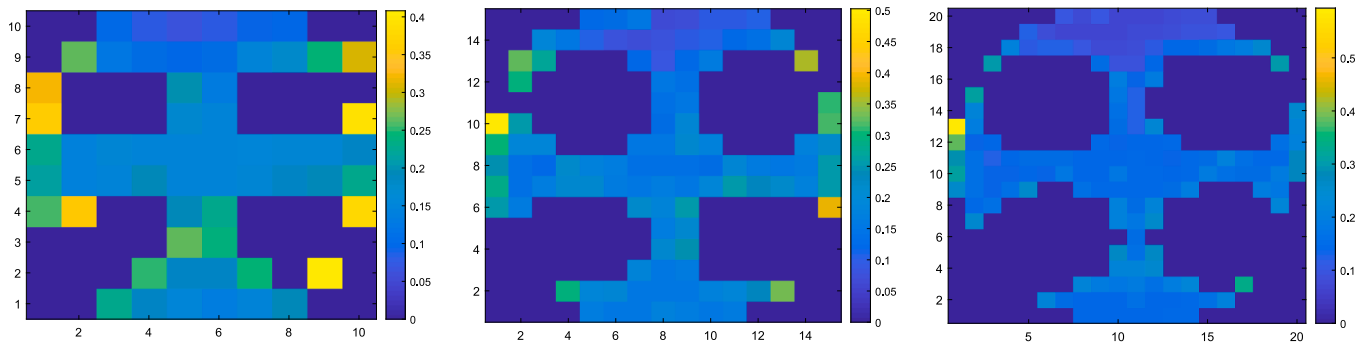


Fig. 11. The converted grayscale image of a combustion chamber surface.



(a) Mean EMD of 10×10 ROIs

(b) Mean EMD of 15×15 ROIs

(c) Mean EMD of 20×20 ROIs

Fig. 10. The mean EMD in each ROI of in-control samples.

Table 4
The comparison of ARL1 values of four methodologies.

Defect size	Magnitude of shift	He et al. (2017)	Stankus et al. (2019)	Scimone et al. (2021)	The proposed method
R = 2	+0.3	1.31	1.00	5.45	1.00
	+0.2	1.76	2.75	13.76	1.00
	+0.1	2.82	3.89	47.05	2.23
	-0.1	2.73	4.77	53.82	2.89
	-0.2	1.42	1.21	10.07	1.00
R = 1	-0.3	1.20	1.00	7.37	1.00
	+0.3	1.62	1.00	18.21	1.00
	+0.2	2.85	2.07	55.10	1.54
	+0.1	3.96	5.61	79.12	5.76
	-0.1	5.69	6.87	127.41	4.80
	-0.2	3.77	2.80	48.52	1.96
	-0.3	2.04	1.00	19.51	1.00

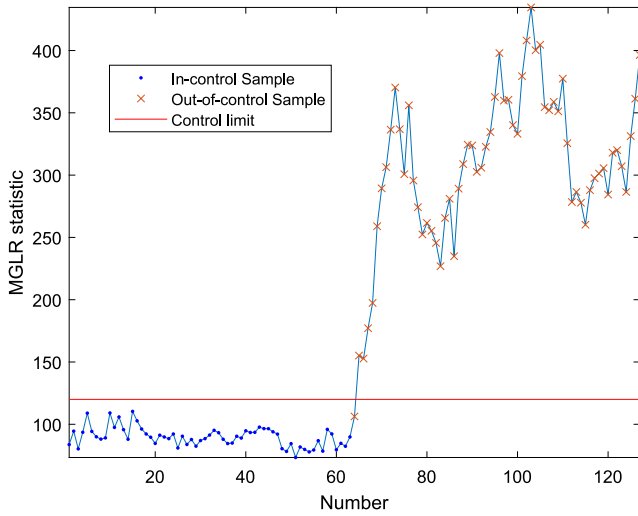


Fig. 12. The monitoring process of the proposed method.

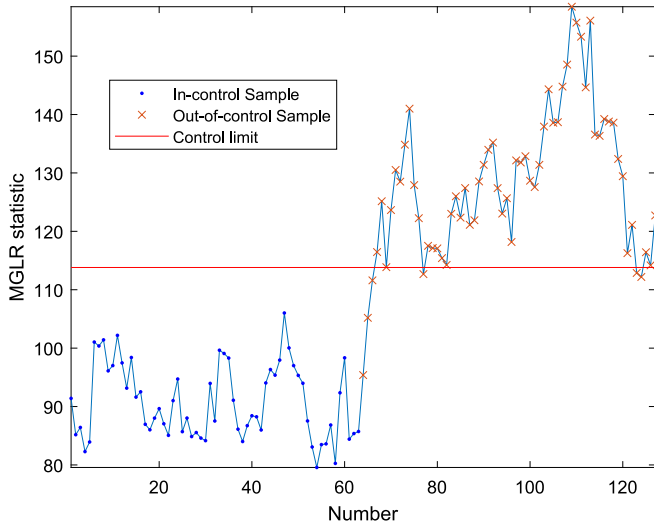


Fig. 13. The monitoring process of He et al. (2017).

3.2. Data preprocessing and regional division

The point cloud data of the engine cylinder head contains the cylinder head plane and combustion chamber surface. In the point cloud

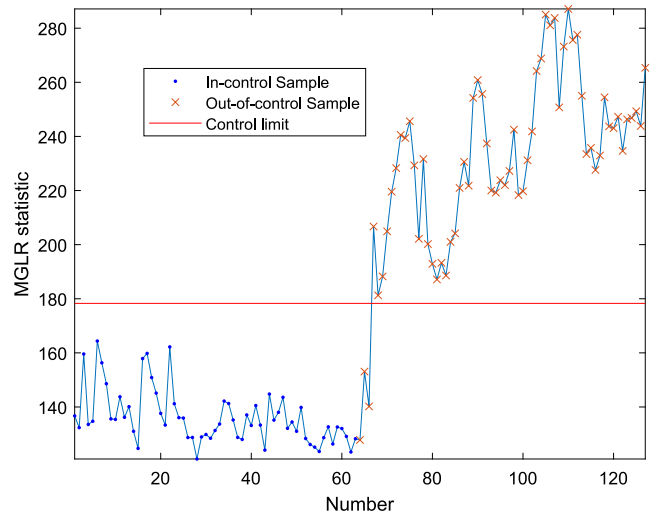


Fig. 14. The monitoring process of Stankus et al. (2019).

preprocessing step, we align the cylinder head surface with the x-y plane, and remove the plane point cloud according to the z coordinate. Then, according to the point cloud processing process in Subsection 2.2, the cylinder head combustion chamber point cloud is processed by removing outliers, filling missing points, and surface registration. The data processing process is shown in Fig. 7.

The next step is to divide the volume occupied by the point cloud into ROIs. ROIs are defined as non-overlapping cubes. First, the coordinate boundaries [x min, x max], [y min, y max], and [z min, z max] are calculated. Then, the numbers of grids m, n, and l are set in the x-axis, y-axis, and z-axis directions. The size of each sub-region is $(\frac{x_{max}-x_{min}}{m} \times \frac{y_{max}-y_{min}}{n} \times \frac{z_{max}-z_{min}}{l})$. In this case, the coordinate boundaries of combustion chamber surface are x[0,70 mm], y[0,62 mm], and z [0,10 mm]. The numbers of ROIs influence the effect of control chart and need to be discussed. Since the combustion chamber surface does not overlap in the z-axis, the z-axis is not divided. The point cloud is divided in the x-axis and y-axis directions. Fig. 8 shows that the point cloud data of a combustion chamber surface is divided into 10 × 10 ROIs.

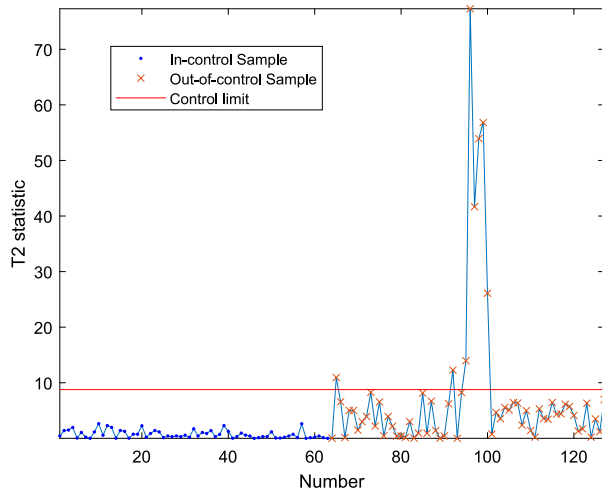
3.3. Numerical experiment

3.3.1. Phase I of MGLR control chart

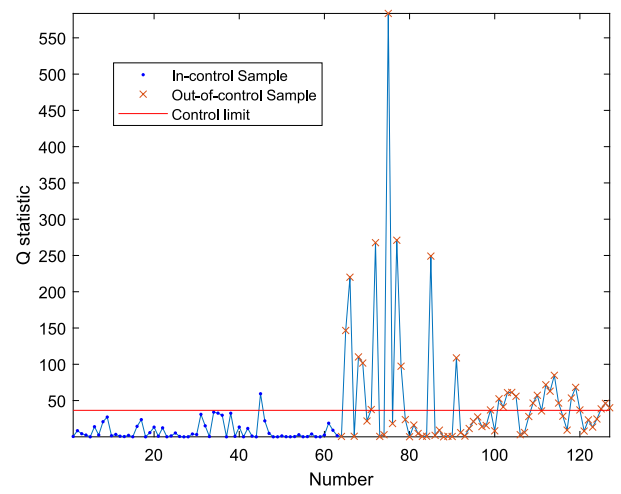
In Phase I, the control chart is established under the stable process, and the control limit of the control chart is calculated through simulation. A random term is added to the real measurement point clouds as simulation samples to set up the MGLR control chart. In the z-axis direction, a noise value that obeys Gaussian distribution with the mean of 0 and the standard deviation of 0.02 is added. The control limit of MGLR control chart is designed through the following steps:

- Step 1: Select an initial value of control limit h. Calculate MGLR statistics for a group of simulation data. When the statistic of the ith sample $R_i > h$, stop the calculation and record the current run length (RL). Calculate the next group of samples and repeat this process until all groups are processed. Calculate the average run length (ARL) of all groups.
- Step 2: Compare the ARL with the target value ARL_0 . If $ARL > ARL_0$, decrease h; If $ARL < ARL_0$, increase h.
- Step 3: Recalculate the ARL value according to the updated h. Repeat this step until $ARL \approx ARL_0$. The corresponding h value is regarded as the control limit of MGLR control chart.

In this experiment, the in-control average run length is set as $ARL_0 =$



(a) T^2 control chart



(b) Q control chart

Fig. 15. The monitoring process of Scimone et al. (2021).

Table 5
The FDR and FAR of the methods in the process monitoring.

	He et al. (2017)	Stankus et al. (2019)	Scimone et al. (2021)	The proposed method
FDR	0.906	0.953	0.547	0.984
FAR	0	0	0.016	0

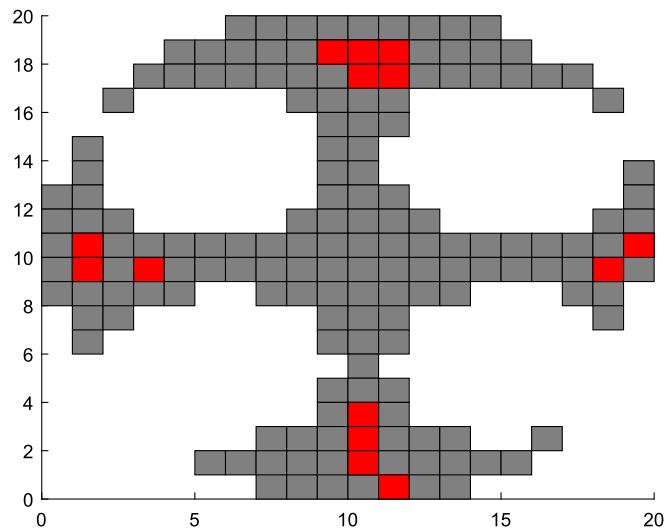


Fig. 16. Measurement points. The red areas are the defects. (For interpretation of the references to colour in this figure legend, the reader is referred to the web version of this article.)

200. 1000 samples are generated for each group, and 1000 groups are simulated to obtain the control limit of MGLR control chart.

In addition, in the MGLR control chart, two conditional parameters (the number of past scans and the number of ROIs) are related to the calculation of the MGLR statistics and need to be optimized.

A small number of past scans, m (in formula (6)), cannot immediately identify defects, while a large m increases the computational burden, especially when the number of ROIs is large. He et al. (2017) discussed $m = 10$ as the literature standard. He et al. (2016), Pacella et al. (2017),

and Stankus et al. (2019) all used $m = 10$ as the standard value of past scans considering the convenience of calculation and the ability to quickly identify defects. In this experiment, therefore, $m = 10$ is selected as the number of past scans.

With a small number of ROIs, it is difficult to quickly identify small defects and impossible to accurately locate the defect location; a large number of ROIs will make it difficult to calculate large-scale metrics. The selection of ROIs is also different for different measurement samples. For the measurement samples used in this experiment, three ROIs of 10×10 , 15×15 , and 20×20 are chosen to be discussed, because they can quickly find process shifts and have a relatively short computation time. The control limits of three ROIs are calculated and shown in Table 1.

The control limits are obtained by establishing the control charts of phase I and utilized in Phase II for process monitoring. The next subsection describes the application of the proposed method in Phase II by artificially adding defects.

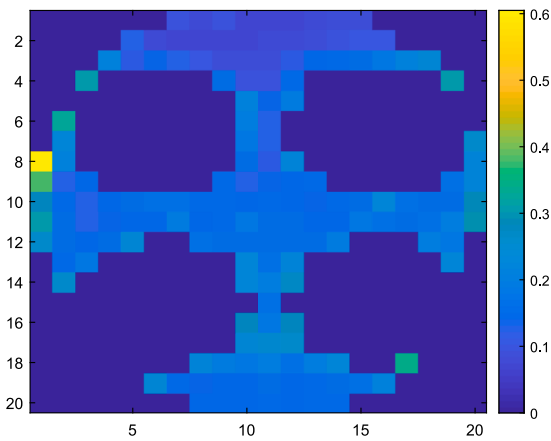
3.3.2. Phase II of MGLR control chart

In the casting process, the wear of the die will cause surface dents. The simulated dent defects are added to the in-control point clouds for testing. Fig. 9 shows the diagram of in-control point clouds with red-marked defects areas and the arrow-marked locations of defect centers. As shown in Fig. 9, circular dents are added at five random locations, where the depth is 0.2 mm and the radius is 2 mm or 1 mm.

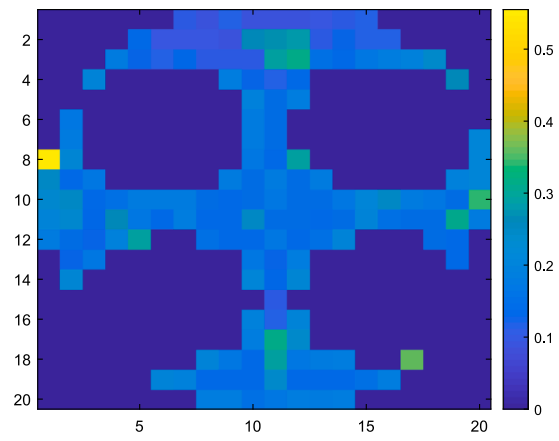
In Phase II, the simulated defects in Fig. 9 are added to the simulation as out-of-control samples. 1000 defect samples are generated, and the simulation is repeated 1000 times in each condition. ARL1 values are compared in three ROIs of 10×10 , 15×15 , and 20×20 (shown in Table 2).

The number of ROIs has a significant impact on the ARL1 value. The greater the number of ROIs (i.e., the smaller the area size), the more effective the monitoring of the control chart. Similarly, the larger the defect size, the more accurate the recognition of the control chart. Therefore, the size of ROI depends on the expected size of the defects. The monitoring effect for large defect size is higher than that for small defect size. In the proposed method, the case of 15×15 ROIs has an effective result for the defect size of $R = 2$, while it needs 20×20 ROIs for $R = 1$. Therefore, in practice, if the expected size of the defects is small, then a larger number of ROI is required. Meanwhile, the effect of the proposed method is significantly improved with the increase of the number of ROI.

In the same size of defects, ARL1 values have differences in different



(a) Mean EMD of qualified samples



(b) Mean EMD of unqualified samples

Fig. 17. The EMD values of qualified and unqualified samples.

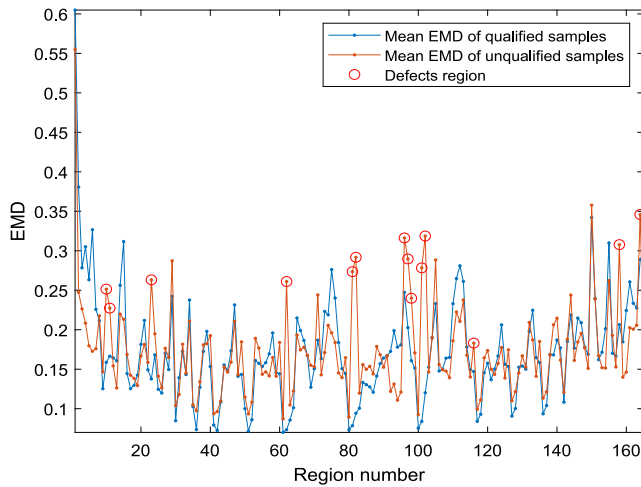


Fig. 18. Plot for mean EMD of qualified and unqualified samples.

defect locations. Control charts can quickly identify the shift when the defect location is in the center of the surface: (34, 30), which is related to the sample shape and measurement error. Fig. 10 is the mean EMD value of each ROI calculated from the in-control samples. The EMD at the edge is large, which shows that the fluctuation of the measurement data is large in these regions. This is because the shape of combustion chamber surface. The large inclination angle of the edge of the measured surface affects the imaging of the laser scanning line. In the center position, the measured surface is closer to the plane, and the measurement accuracy is higher compared with the edge position. As the number of ROIs increases, the EMD value of the surface becomes smoother, and so the recognition of defects is more effective. Table 2 and Fig. 10 discuss the effect of ROI size, defects size, and location on the control chart. The 20×20 ROI has the best results and is performed in the MGLR control chart.

Next, the influence of the magnitude of shift on the control chart effect is discussed. The 20×20 ROI is performed in the MGLR control chart. The dents (magnitude is positive) and bulges (magnitude is negative) are added to the simulation samples as defects. The magnitudes of shifts are -0.3 mm, -0.2 mm, -0.1 mm, $+0.1$ mm, $+0.2$ mm, and $+0.3$ mm. The ARL1 values are shown in Table 3.

Table 3 discusses the size, location, and magnitude of defects. Same to Table 2, the monitoring effect of control chart for large defect size is

better than that for small defect size. The monitoring effect of the central areas is better than that of edge areas. In addition, for the magnitude of shift, the monitoring effect of the large shifts is better than that of the small shifts. In the listed cases, magnitude of shift has a greater impact on the control chart monitoring effect than defect size.

3.4. Method comparison

The proposed EMD-MGLR method is compared with three state-of-the-art methods proposed by He et al. (2017), Stankus et al. (2019), and Scimone et al. (2021). The first two methods are also based on the MGLR control chart, and the last method is based on the Hausdorff distance. In the method comparison, the same ARL0 value is set in the in-control process, and the ARL1 values are compared in Phase II. In Phase II, the defect samples of all five defect types in Fig. 9 are simulated.

He et al. (2017) converted point cloud data into grayscale images through 2D mapping and monitored the grayscale values. In this method, the point clouds are converted into grayscale values, as shown in Fig. 11. Height values of point clouds are converted to the interval [0, 255]. Each grayscale image is divided into 20×20 ROIs. The mean of the gray values in each ROI is calculated and then monitored by the MGLR control chart.

The method proposed by Stankus et al. (2019) is to calculate the deviation value between the measurement point and the standard surface, convert the deviation value through Fast Fourier transform, and monitor the mean deviation value of each ROI through the MGLR control chart. To facilitate comparison, the same qualified sample is selected as the nominal surface. The distance between the point on the measured sample and the closest point on the nominal surface is calculated as the deviation value.

Scimone et al. (2021) used Hausdorff distance to model the deviation between the measurement sample and the nominal sample. They performed principal component analysis on probability density functions of Hausdorff distance, and then monitored the geometric differences of the measured samples through T^2 and Q control charts. They used this method to monitor structural defects in 3D printing, benefiting from the sensitivity of the Hausdorff distance to extreme points. In this method, T^2 and Q statistics are used to represent the quality characteristics of the measured samples, and region segmentation is not required.

Set $ARL0 = 200$ for all methods, i.e., type I error $\alpha = 0.005$. In Phase II, 1000 samples with defects are simulated (each defect sample includes all five defect types in Fig. 9) and are repeated 1000 times. The ARL1 value of each situation is shown in Table 4.

Among these four methods, the proposed method has the minimum

ARL1 value in most cases. The method proposed by He et al. (2017) is effective in the case of small shift, the method proposed by Stankus et al. (2019) is effective in the case of large shift, while the method proposed by Scimone et al. (2021) is difficult to identify the small shift. The proposed method is effective for both large shift and small shift. In the case of different defect sizes, the recognition effect of these four methods for large defect size is better than that for small defect size. The method proposed by He et al. (2017) is insensitive to defect size changes, and the recognition effect is not as good as the proposed method when the defect size is large.

4. Process monitoring and further analysis

The proposed method is implemented on process monitoring to emphasize how it can be used in practice.

4.1. Process monitoring

The traditional detection method for the combustion chamber is to regularly inspect the mold through a coordinate measuring machine (CMM). The technician manually selects the measurement position and quantity of the combustion chamber mold and evaluates the surface quality through engineering experience. The results are then compared with the model in the z-axis direction to determine whether the z-direction deviation of each measuring point is within ± 0.3 mm. Deviation beyond this range indicates that the area near this point is defective. When the number of unqualified points is large, the combustion chamber is considered unqualified. In this process, the number and the location of measuring points and the quality evaluation are all based on engineering experience. However, this method has a long measurement time and high cost and can only take measurements at intervals, which easily leads to engineering losses. In the production process, 64 unqualified combustion chambers were produced due to mold wear. These samples are measured in HDM and compared with the measured qualified samples by using the proposed method.

In this study, 64 qualified samples and 64 worn combustion chamber samples were measured by the 3D line laser scanner. The first qualified sample was taken as the nominal sample. 20×20 ROIs and the simulated control limit in Subsection 3.3.1 are utilized. The method is applied to process monitoring, in which the production process is out of control after the 63rd sample.

The monitoring process of the proposed method is shown in Fig. 12. The process shift is identified from the second unqualified sample. In addition, out of 64 unqualified samples, 63 unqualified samples are identified by this method. In the actual machining process, this method can quickly identify the process shift and accurately identify the unqualified samples.

4.2. Method comparison

The three state-of-the-art methods introduced in Subsection 3.4 are also used for comparisons with the proposed EMD-MGLR method in this process monitoring study.

For the methods of He et al. (2017) and Stankus et al. (2019), the MGLR control charts are established and the 20×20 ROIs are selected, whereas the method of Scimone et al. (2021) is based on T^2 and Q control charts for process monitoring. The statistics of 127 samples are computed for all three methods, and the control charts are established for process monitoring, as shown in Figs. 13-15.

The method proposed by He et al. (2017) (Fig. 13) identifies the process shift at the fourth unqualified sample, and 58 of the 64 unqualified samples are identified. The method proposed by Stankus et al. (2019) (Fig. 14) identifies the process shift at the fourth unqualified sample, and 61 of the 64 unqualified samples are identified. The method proposed by Scimone et al. (2021) (Fig. 15) identifies the process shift at the second unqualified sample, and 35 of the 64 unqualified samples are

identified.

To assess the results of each method, false detection rate (FDR) and false alarm rate (FAR) are adopted, which can be calculated by:

$$FDR = \frac{\text{The number of false samples correctly detected}}{\text{Total number of false samples}}$$

$$FAR = \frac{\text{The number of normal samples distinguished as false samples}}{\text{Total number of normal samples}}$$

Table 5 shows the FDR and FAR results of the three comparison methods and the proposed method.

The proposed method has the highest FDR. Compared with the three state-of-the-art methods, the true detection rate of unqualified samples is improved by 8.6 %, 3.3 % and 79.9 % respectively. The values of FAR are all 0 except for the method of Scimone et al. (2021). Compared with other methods, the proposed method can identify the process shift fastest and has the highest detection rate for unqualified samples.

4.3. Defect region identification

In the proposed method, each sample is divided into non-overlapping cube regions. Because the division is based on spatial volume, this method can provide a reference for defect region recognition. Comparing the results of the proposed method and the measurement of CMM, the identification of defect regions is discussed.

The worn mold is inspected by CMM, and the detection result is shown in Fig. 16. The detection points are evenly distributed in the x-axis and y-axis directions. Each region represents a measurement position. Since some areas associate with missing measurement points, only the areas with valid measurement points in both methods are compared. Fig. 17 shows the mean EMD values of the qualified and unqualified samples based on HDM. For comparison, the EMD values are converted into a vector form by column arrangement, as shown in Fig. 18.

The mean EMD of qualified and unqualified samples are calculated and compared in Fig. 18. The blue line represents the mean EMD value of the 20×20 ROIs calculated from the 63 in-control point clouds, the red line represents the mean EMD value of the 64 unqualified samples, and the red circles indicate defect regions previously shown in Fig. 16. In the defect regions, the EMD value of the unqualified sample deviates significantly from the EMD value of the qualified sample, and the defect regions can be identified. However, in some regions, such as the 71st, and 105th regions, the EMD of the unqualified sample is also significantly larger than the mean EMD of the qualified samples. There are three possibilities: (1) Due to the characteristics of the samples and HDM, the shape of these regions fluctuates greatly, and the EMD values in these regions have a large variance. (2) As CMM only measures one point in each ROI, it cannot represent the whole region, thereby increasing the risk of misjudgment. (3) CMM measures the mold to indirectly reflect the quality of the part, which is different from the actual shape of the part surface. In general, the EMD values of the measured samples can provide a reference for identifying and determining the location of surface defects.

5. Conclusions

In this paper, an EMD-MGLR method is proposed for surface monitoring of 3D point clouds to quickly identify and locate surface defects. With point cloud data, the proposed method calculates the EMD value to represent the difference between the measured surface and the nominal surface. To identify the process shifts, the 3D surface is divided into ROIs, and the EMD value of each ROI is monitored through MGLR based control chart. This method can satisfy the required efficiency for calculation of point cloud data with large-scale characteristics and can effectively identify process shifts, which provides a reference for the identification and location of surface defects. In numerical experiments,

the proposed method is validated by actual measured data of engine cylinder head combustion chambers. The experimental results show that the proposed method outperforms the state-of-the-art methods in identifying the process shift. In the process monitoring study, the proposed method rapidly identifies the process shift and gives the highest detection rate for unqualified samples. In addition, the proposed method does not require projection nor image transformation of 3D point clouds or a known CAD model. Thus, it can be applied to point cloud surfaces of arbitrary shapes. Moreover, in this experiment, the ROIs' positions are divided along the x-axis and y-axis, and all regions are assumed to be the same size. For more complex surface shapes, ROIs can also be divided along the z-axis. There are several possible directions for future research:

- (1) Currently, only offline measured data has been used for analysis. The proposed method can be combined with online HDM to establish control charts based on historical data for online monitoring, thereby providing real-time feedback on the process.
- (2) The proposed method is based on the MGLR control chart and can identify the mean shift. The method of the control chart could be further studied to monitor other types of process changes, for example, changes in covariance.

Declaration of Competing Interest

The authors declare that they have no known competing financial interests or personal relationships that could have appeared to influence the work reported in this paper.

Data availability

The authors do not have permission to share data.

Acknowledgments

This work was supported by the National Natural Science Foundation of China (Grant No. 52275499) and National key R&D plan of China (No. 2022YFF0605700). This work was partially supported by Hong Kong Innovation and Technology Commission (InnoHK Project CIMDA).

References

- Besl, P. J., & McKay, N. D. (1992). A method for registration of 3-D shapes. *IEEE Transactions on Pattern Analysis and Machine Intelligence*, 14(2), 239–256.
- Chazal, F., Cohen-Steiner, D., & Mérigot, Q. (2010). *Geometric inference for measures based on distance functions*. RR-6930. INRIA Research Report,.
- Du, S., Liu, C., & Huang, D. (2015). A shearlet-based separation method of 3D engineering surface using high definition metrology. *Precision Engineering*, 40, 55–73.
- He, K., Zhang, M., Zuo, L., Alhwiti, T., & Megahed, F. M. (2017). Enhancing the monitoring of 3d scanned manufactured parts through projections and spatiotemporal control charts. *Journal of Intelligent Manufacturing*, 28(4), 899–911.
- He, Z., Zuo, L., Zhang, M., & Megahed, F. (2016). An Image-based Multivariate Generalized Likelihood Ratio Control Chart for Detecting and Diagnosing Multiple Faults in Manufactured Products. *International Journal of Production Research*, 54(6), 1771–1784.
- Jia, D., Zhang, W., Wang, Y., & Liu, Y. (2021). A New Approach for Cylindrical Steel Structure Deformation Monitoring by Dense Point Clouds. *Remote Sensing*, 13(12), 2263.
- Megahed, F., Wells, L., Camelio, J., & Woodall, W. (2012). A Spatiotemporal Method for the Monitoring of Image Data. *Quality and Reliability Engineering International*, 28(8), 967–980.
- Mukherjee, A., & Marozzi, M. (2021). Nonparametric Phase-II control charts for monitoring high-dimensional processes with unknown parameters. *Journal of Quality Technology*, 54(1), 44–64.
- Pacella, M., & Colosimo, B. M. (2018). Multilinear Principal Component Analysis for Statistical Modeling of Cylindrical Surfaces: A Case Study. *Quality Technology & Quantitative Management*, 15, 507–525.
- Pacella, M., Grieco, A., & Blaco, M. (2017). Machine vision based quality control of free-form profiles in automatic cutting processes. *Computers & Industrial Engineering*, 109, 221–232.
- Rubner, Y., Tomasi, C., & Guibas, L. J. (1998). A metric for distributions with applications to image databases. *IEEE Computer Society. Proceedings of the 1998 IEEE International Conference on Computer Vision*, Bombay, India.
- Scimone, R., Taormina, T., Colosimo, B. M., Grasso, M., & Secchi, P. (2021). Statistical modeling and monitoring of geometrical deviations in complex shapes with application to additive manufacturing. *Technometrics, Ahead-of-print*, 1–20.
- Shu, L., & Fan, J. (2018). A Distribution-free Control Chart for Monitoring High-dimensional Processes Based on Interpoint Distances. *Naval Research Logistics*, 65(4), 317–330.
- Solomon, J., Rustamov, R., Guibas, L., & Butscher, A. (2014). Earth mover's distances on discrete surfaces. *ACM Transactions on Graphics*, 33(4), 1–12, 67.
- Stankus, S. E., & Castillo-Villar, K. K. (2019). An Improved multivariate generalised likelihood ratio control chart for the monitoring of point clouds from 3D laser scanners. *International Journal of Production Research*, 57(8), 2344–2355.
- Wang, S., & Reynolds, M. (2013). A GLR Control Chart for Monitoring the Mean Vector of a Multivariate Normal Process. *Journal of Quality Technology*, 45(1), 18–33.
- Wells, L. J., Megahed, F. M., Niziolek, C. B., Camelio, J. A., & Woodall, W. H. (2013). Statistical process monitoring approach for high-density point clouds. *Journal of Intelligent Manufacturing*, 24(6), 1267–1279.
- Williams, J. D., Woodall, W. H., & Birch, J. B. (2007). Statistical monitoring of nonlinear product and process quality profiles. *Quality and Reliability Engineering International*, 23(8), 925–941.
- Yan, H., Paynabar, K., & Pacella, M. (2019). Structured Point Cloud Data Analysis Via Regularized Tensor Regression for Process Modeling and Optimization. *Technometrics*, 61(3), 385–395.
- Yin, Y., Shao, Y., Wang, K., Du, S., & Xi, L. (2020). Segmentation of workpiece surfaces with tool marks based on high definition metrology. *Journal of Manufacturing Processes*, 57, 268–287.
- Zang, Y., & Qiu, P. (2018a). Phase I Monitoring of Spatial Surface Data from 3D Printing. *Technometrics*, 60(2), 169–180.
- Zang, Y., & Qiu, P. (2018b). Phase II monitoring of free-form surfaces: An application to 3D printing. *Journal of Quality Technology*, 50(4), 379–390.
- Zhang, C., Chen, N., & Wu, J. (2019). Spatial Rank based High-dimensional Monitoring Through Random Projection. *Journal of Quality Technology*, 52(2), 111–127.
- Zhao, C., Cheung, C., & Liu, M. (2019). Nanoscale measurement with pattern recognition of an ultra-precision diamond machined polar microstructure. *Precision Engineering*, 56, 156–163.
- Zhao, C., Du, S., Lv, J., Deng, Y., & Li, G. (2021). A novel parallel classification network for classifying three-dimensional surface with point cloud data. *Journal of Intelligent Manufacturing*, 08–11.
- Zhao, C., Xi, Y., Shao, Y., Xue, W., Deng, D., & Wu, Y. (2022). Investigation and optimization of a novel precision measurement method based on template-matching. *Measurement Science and Technology*, 33, Article 085017.